IOPscience iopscience.iop.org

Home Search Collections Journals About Contact us My IOPscience

Reconstruction of structural damage based on reflection intensity spectra of fiber Bragg gratings

This content has been downloaded from IOPscience. Please scroll down to see the full text.

2014 Meas. Sci. Technol. 25 125109

(http://iopscience.iop.org/0957-0233/25/12/125109)

View the table of contents for this issue, or go to the journal homepage for more

Download details:

IP Address: 159.226.231.70
This content was downloaded on 04/01/2015 at 02:13

Please note that terms and conditions apply.

IOP Publishing Measurement Science and Technology
Meas. Sci. Technol. **25** (2014) 125109 (19pp) doi:10.1088/0957-0233/25/12/125109

Reconstruction of structural damage based on reflection intensity spectra of fiber Bragg gratings

Guojun Huang, Changben Wei, Shiyuan Chen and Guowei Yang

Institute of Mechanics, Chinese Academy of Sciences, 15, Beisihuanxi Road, 100190, Beijing, People's Republic of China

E-mail: ghuang@imech.ac.cn

Received 24 June 2014, revised 15 September 2014
Accepted for publication 30 September 2014
Published 31 October 2014

Abstract

We present an approach for structural damage reconstruction based on the reflection intensity spectra of fiber Bragg gratings (FBGs). Our approach incorporates the finite element method, transfer matrix (*T*-matrix), and genetic algorithm to solve the inverse photo-elastic problem of damage reconstruction, i.e. to identify the location, size, and shape of a defect. By introducing a parameterized characterization of the damage information, the inverse photo-elastic problem is reduced to an optimization problem, and a relevant computational scheme was developed. The scheme iteratively searches for the solution to the corresponding direct photo-elastic problem until the simulated and measured (or target) reflection intensity spectra of the FBGs near the defect coincide within a prescribed error. Proof-of-concept validations of our approach were performed numerically and experimentally using both holed and cracked plate samples as typical cases of plane-stress problems. The damage identifiability was simulated by changing the deployment of the FBG sensors, including the total number of sensors and their distance to the defect. Both the numerical and experimental results demonstrate that our approach is effective and promising. It provides us with a photo-elastic method for developing a remote, automatic damage-imaging technique that substantially improves damage identification for structural health monitoring.

Keywords: damage reconstruction, fiber Bragg grating, reflection intensity spectrum, transfer matrix, genetic algorithm, finite element method

(Some figures may appear in colour only in the online journal)

1. Introduction

Fiber Bragg gratings (FBGs) offer optical sensors for strain and temperature that are lightweight, small in size, immune to electro-magnetic interference, highly sensitive, etc [1]. Most prominently, by virtue of wavelength encoding, up to 100 FBGs may be deployed in series along a fiber to realize a quasi-distributed measurement of strain or temperature. Therefore, FBGs have been widely applied for sensing and structural health monitoring (SHM) [2, 3].

So far, FBGs have experienced three major technical advances in their applications to strain sensing and structural damage detection. First, in the most common current application, the FBG is used as a point-wise sensor, which collects only the central/peak wavelength shift in the reflection intensity spectrum, to measure the average strain over the grating length of the FBG. Although limited information on the structural response is gained from this FBG, a quasi-distributed measurement of strain can be achieved by virtue of wavelength encoding, and thus an FBG sensing net can be realized for SHM.

The second development is the realization of truly distributed strain measurement over the grating length. In this sensing application, complete reflection spectrum information of the FBG, involving not only the shift but also the distortion of the spectrum, is used to reconstruct the strain profile over

 © 2014 IOP Publishing Ltd Printed in the UK

the grating length. To save cost, this approach is mainly based on the intensity spectrum approach [4–10]. Meanwhile, phase spectrum [11] and complex spectra (i.e. intensity and phase spectra) approaches [12, 13] have also been proposed. As a result, an FBG could be used as a line-wise sensor to obtain the local strain gradient in addition to the local strain of the structures.

Third, in recognition that structural defects always accompany nearby stress concentrations, which induces a high strain gradient and remarkably affects the profile of the reflection spectrum, FBGs have been further used to detect structural damage [14–20]. In this application, FBGs are imbedded into the structure, near the defect or damage zones. The empirical correlation can then be investigated experimentally or theoretically between the reflection intensity spectra and the indices characterizing the various known defects. In this way, an empirical database is established and then used for damage identification. However, because the reflection intensity spectrum is affected not only by the size and shape of the defect itself but also by its distance to the deployed FBG sensors, the database could be extensive in general. Therefore, the FBG-based defect detection has been limited mainly to recognize the existence of damage.

The present work is devoted to the development of a theoretical approach for reconstructing structural damage from the reflection intensity spectra of FBGs, which is also an extension of the FBG-based strain profile reconstruction. By this approach, all of the defect geometry, not only the size and shape but also the location of the defect, is theoretically deduced from the reconstructed strain profiles or directly from the measured reflection intensity spectra of FBGs, rather than determined from an empirical damage database. Indeed, the latter involves only the direct problem of damage detection, while our damage reconstruction constitutes its inverse problem, as described in detail in section 3. Although many investigations have studied the direct problem, the inverse problem has rarely been studied. To the best of our knowledge, only Taketa *et al* [21, 22]. have attempted to address this inverse problem of reconstructing the damage patterns near the notch and hole of composite laminates. Some preliminary assumptions, however, regarding the damage geometry such as the defect shape or the size of the damage zone were made in their inversion calculations. The feasibility of the damage reconstruction based on FBGs still requires a systematical study. Our work is to develop a general approach for damage reconstruction, without a preliminary assumption regarding the defect geometry,

In addition to above-mentioned intention on enriching FBG sensing technology and application, the present work is also motivated by an desire to devise an automatic and remote technique for nondestructive evaluation (NDE), with damage imaging capabilities, meeting the *in-situ* and on-time monitoring requirements of SHM. Structural damage identification plays a vital role in both SHM and the conventional regular inspection. Damage reconstruction is the highest level of damage identification owing to its capability of not only recognizing the existence of damage in a structure but also determining the shape, size, and location of the defect, hence realizing damage imaging. Ultrasound, x- or gamma-rays, etc, are the most popular NDE techniques with damage reconstruction/imaging capabilities, applied broadly in material and structural damage inspections and medical imaging. In these NDE techniques, damage reconstruction is based on the transmission, diffraction, refraction scattering, and reflection of acoustic/elastic and electromagnetic waves, respectively [23–28]. Damage images are generated by 1D or 2D transducer scans in these dynamical approaches. Therefore, they rely on manual operation in general and, thus, are applied only in the regular inspection. Even then, for the structural sites human can not reach at, such as the interior of nuclear reactor and deep water structures, damage inspection is difficult to conduct using these NDE techniques. SHM is superior to the conventional regular inspection in saving maintenance cost and in increasing structural safeguarding capabilities [29]. However, since the point-wise strain, velocity, acceleration, etc, are main measurands of structural response, damage identifiability of SHM is inferior to the regular inspection. Especially, damage reconstruction is not realized by the present SHM technique nowadays. Our damage reconstruction is a static approach, based upon the inversion from the part information on the static nonhomogeneous distributed strain field around the structural defect near the FBGs, which is obtained from the reflection intensity spectra of the FBGs that can be collected in an automatic and remote way. Hence, this will provide us with a novel NDE technique with damage imaging capabilities and suitable to SHM. If applied at the hotspots of engineering structures, it will greatly enhance the damage identifiability of SHM. The present approach combines the superiors of SHM and the conventional NDE techniques.

Mechanical damage reconstruction is a typical inverse problem in elasticity. Several theories and algorithms have been formulated for the reconstruction of cracks or voids, e.g. the reciprocity gap (RG) functional, error in constitutive equation (ECE) functional, adjoint state and topological derivative [30]. Damage reconstruction can be made either from solving the observation equations, which relate the complete/field measurements of both traction and displacement on the full boundary surface of structures to the unknown damage quantities, or from the minimization of a cost functional that embodies a definition of the 'best fit' between the partial measurement data and simulated data. Indeed, the latter is an approximation inversion. More measurement information generates more accurate damage reconstruction. The complete field measurement on the full boundary, however, is difficult to conduct and the partial or discrete measurement is practical. In the present approach, although truly distributed strain measurements can be realized along the gratings of FBGs, it is still limited information, compared with the complete field measurement. Thus, a basic issue arises that is how many FBGs are needed for reconstructing a structural defect within a practically allowable precision. This is just the issue of damage identifiability. Besides, the damage identifiability is affected also by the damage mode (voids or cracks) and the relative distance of FBGs to the defect center, scaled by the defect size. In the present work, the damage identifiability

was evaluated by changing these factors. As a starting point for this research, our work was confined to the plane problem.

In what follows, the wave-guide theory of an optic fiber on the reflection intensity spectrum of FBGs is outlined in section 2, which is the basic optical theory of our damage reconstruction. Then, the direct and corresponding inverse photo-elastic problems of damage reconstruction, together with the relevant formulas, are described in section 3, and an optimization approach for the solution to the inverse photo-elastic problem is presented in section 4. Next, numerical and experimental proof-of-concept validations of our approach, which evaluate the damage identifiability, are presented in sections 5 and 6, respectively. Finally, our work is summarized in section 7.

2. Reflection intensity spectra of FBGs

An FBG can be characterized by the core refractive index of the guided mode that has its axial non-uniformity described by the following function [5]:

$$n(z)= n_0 + \delta n(z)+ \Delta n(z)\cos\left[\frac{2\pi}{\Lambda_0}z + \phi(z)\right], \tag{1}$$

where z is the axial coordinate of the fiber, and $\delta n(z)$ indicates the 'dc' perturbation, which is spatially averaged over a grating period, relative to the unperturbed constant core refractive index n_0, and involves the effects of the grating fabrication process and possible external influences such as strain or temperature. In addition, $\Delta n(z)$ denotes the index modulation amplitude, and $\phi(z)$ stands for the index modulation phase that reflects a possible chirp to the unperturbed grating period Λ_0.

Based on mode-coupling theory, quantitative information about the reflection spectrum of a single-mode FBG can be obtained by solving the following differential equations, called mode-coupling equations [31]:

$$\begin{cases} \dfrac{\mathrm{d}R(z)}{\mathrm{d}z} = \mathrm{i}\hat{\sigma}R(z)+\mathrm{i}\kappa S(z) \\ \dfrac{\mathrm{d}S(z)}{\mathrm{d}z} = -\mathrm{i}\hat{\sigma}S(z)-\mathrm{i}\kappa R(z) \end{cases}, \tag{2}$$

where $R(z)$ and $S(z)$ are the field amplitudes of the forward and backward guided modes, respectively, $\hat{\sigma}$ is a general 'dc' self-coupling coefficient, and κ is the 'ac' coupling coefficient. For the single-mode FBG, $\hat{\sigma}$ and κ are defined as

$$\hat{\sigma} = \delta + \frac{2\pi}{\lambda}\delta n(z) - \frac{1}{2}\frac{\mathrm{d}\phi(z)}{\mathrm{d}z} \tag{3}$$

and

$$\kappa = \frac{\pi}{\lambda}\Delta n(z), \tag{4}$$

where λ is the wavelength. Here, δ is the detuning parameter, expressed as

$$\delta = \frac{2\pi}{\lambda}n_0 - \frac{\pi}{\Lambda_0} = 2\pi n_0\left(\frac{1}{\lambda} - \frac{1}{\lambda_\mathrm{B}}\right), \tag{5}$$

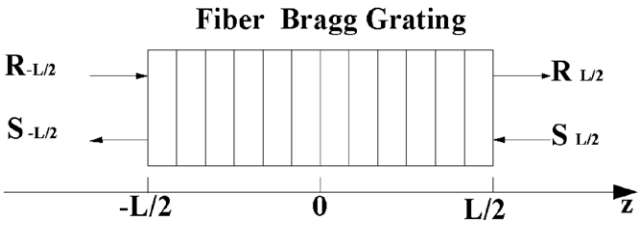

Figure 1. Divisions of an FBG grating.

with the Bragg wavelength $\lambda_\mathrm{B} = 2n_0\Lambda_0$, which is also called the design wavelength.

For non-uniform FBGs, since $\hat{\sigma}$ and κ are z-dependent coefficients, solving equation (2) in general requires direct numerical integration. However, for uniform FBGs, $\hat{\sigma}$ and κ are constant coefficients, and a closed-form analytical solution to equation (2) can be obtained when appropriate boundary conditions are specified at the ends of the grating of length L. Thanks to this analytical solution for uniform FBGs, another approach, termed the T-matrix approach, was proposed [32] to solve equation (2) approximately for non-uniform FBGs. The T-matrix approach is a piecewise-uniform approach in which an FBG can be viewed as an assembly of many piecewise-uniform sections. Thus, for each section, the closed-form solution for uniform FBGs could be used, resulting in a 2×2 T-matrix that relates the input, transmission, and reflection field amplitudes for the given section. Consequently, the overall solution can be obtained by multiplying all of these matrices. This approach is faster, easier to implement, and gives a solution that is almost indistinguishable from one based on the direct numerical integration approach. Therefore, we use the T-matrix approach in our work.

As shown in figure 1, we divide the grating into N uniform sections and define R_i and S_i as the field amplitudes after light traverses the ith section. Thus, we initialize $R_0 = R(L/2) = 1$ and $S_0 = S(L/2) = 0$ and calculate $R_\mathrm{N} = R(-L/2)$ and $S_\mathrm{N} = S(-L/2)$. Propagation through the ith section is described by a matrix $\mathbf{T}_i$ defined by

$$\begin{bmatrix} R_i \\ S_i \end{bmatrix} = \mathbf{T}_i \cdot \begin{bmatrix} R_{i-1} \\ S_{i-1} \end{bmatrix}. \tag{6}$$

This so-called T-matrix has the following full expression [31]:

$$\mathbf{T}_i = \begin{bmatrix} \cosh(\gamma\Delta z) - \mathrm{i}\dfrac{\hat{\sigma}}{\gamma}\sinh(\gamma\Delta z) & -\mathrm{i}\dfrac{\kappa}{\gamma}\sinh(\gamma\Delta z) \\ \mathrm{i}\dfrac{\kappa}{\gamma}\sinh(\gamma\Delta z) & \cosh(\gamma\Delta z) + \mathrm{i}\dfrac{\hat{\sigma}}{\gamma}\sinh(\gamma\Delta z) \end{bmatrix}, \tag{7}$$

where Δz is the length of the uniform sections and

$$\gamma = \sqrt{\kappa^2 - \hat{\sigma}^2} \tag{8}$$

in which the coupling coefficients $\hat{\sigma}$ and κ are locally fixed values of the ith section. Thus, with all of the T-matrices for

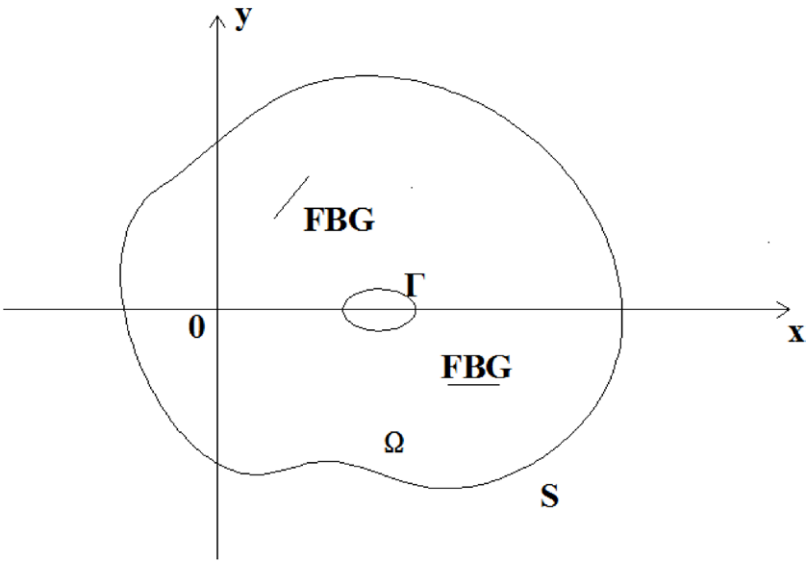

Figure 2. Plane-stress problem of damage reconstruction.

the individual sections being known, one can gain the overall amplitudes

$$\begin{bmatrix} R_N \\ S_N \end{bmatrix} = \mathbf{T} \cdot \begin{bmatrix} R_0 \\ S_0 \end{bmatrix}, \tag{9}$$

with the overall T-matrix

$$T = \mathbf{T}_N \cdot \mathbf{T}_{N-1} \cdot \ldots \mathbf{T}_i \cdot \ldots \cdot \mathbf{T}_0 \,. \tag{10}$$

Then, the power reflection coefficient $\rho = S_N/R_N = T_{21}/T_{11}$ and the reflectivity $r = |\rho|^2$ can be calculated.

When the grating of an FBG is subject to an external longitudinal strain with profile $\varepsilon(z)$, the strain effect on the refraction index can be taken into account by modifying equation (1) as

$$n(z) = n_0 + \delta n(z) + \delta n_\varepsilon(z) + \Delta n(z) \cos\left[\frac{2\pi}{\Lambda_0} z + \phi(z) + \phi_\varepsilon(z)\right], \tag{11}$$

where $\delta n_\varepsilon(z)$ and $\phi_\varepsilon(z)$ describe the strain effects on the mean refractive index and grating period, respectively [5]. They are related to the strain profile $\varepsilon(z)$ as follows:

$$\delta n_\varepsilon(z) = -P_e n_0 \varepsilon(z) \tag{12}$$

and

$$\frac{\mathrm{d}\phi_\varepsilon(z)}{\mathrm{d}z} = -\frac{2\pi}{\Lambda_0^2}\Delta\Lambda(z) = -\frac{2\pi}{\Lambda_0}\varepsilon(z), \tag{13}$$

where we used $\Delta\Lambda(z) = \Lambda_0 \varepsilon(z)$. Here, $\mathrm{Pe} = (n_0^2/2)[(1-\nu)P_{12} - \nu P_{11}]$ is the effective photo-elastic coefficient of the fiber core in which ν is Poisson's ratio, and P_{11} and P_{12} represent the photo-elastic coefficients of the fiber core material. Accordingly, $\delta n(z)$ and $\phi(z)$ in equation (3) are replaced by $\delta n(z) + \delta n_\varepsilon(z)$ and $\phi(z) + \phi_\varepsilon(z)$, respectively.

3. Direct and inverse problems in damage reconstruction

3.1. Elastic

Now, we consider elastic plane-stress problems. Figure 2 shows a damaged plate with unit thickness that occupies an area Ω bounded by external boundary line S and defect contour Γ. Given the elastic properties of the plate body, the geometry of S and Γ, and the boundary conditions, solving the strain or stress field over Ω is then a standard elastic boundary-value problem. The corresponding governing equations without any body forces are given as follows:

Static equilibrium equations $\sigma_{ij,j}(\mathbf{x}) = 0,$ (14)

Constitutive relations $\sigma_{ij}(\mathbf{x}) = C_{ijkl}(\mathbf{x})\varepsilon_{kl}(\mathbf{x}),$ (15)

Compatibility equations $\varepsilon_{ij}(\mathbf{x}) = \frac{1}{2}\left(u_{i,j}(\mathbf{x}) + u_{j,i}(\mathbf{x})\right),$ (16)

where σ_{ij}, C_{ijkl}, and ε_{kl} are the components of the stress, elasticity, and strain tensors, respectively; u_i is a component of the displacement vector; $\boldsymbol{x}$ represents the position vector; and the comma in the subscripts indicates a partial derivative. In addition, the boundary conditions on $1 \times \mathrm{S}$ are, for instance, the displacements ξ_i and traction ϕ_i prescribed respectively on $1 \times \mathrm{S_u}$ and the complementary portion $\mathrm{S_t} = 1 \times (\mathrm{S} \backslash \mathrm{S_u})$:

$$u_i(\mathbf{x}) = \xi_i(\mathbf{x}) \qquad (\mathbf{x} \text{ on } 1 \times S_\mathrm{u}) \tag{17}$$

and

$$t_i = \sigma_{ij}(\mathbf{x}) n_j(\mathbf{x}) = \phi_i(\mathbf{x}) \qquad (\mathbf{x} \text{ on } 1 \times \mathrm{S_t}), \tag{18}$$

where t_i and n_i are the components of traction and the normal vectors of S, respectively. Here, $1 \times \Gamma$ is a free surface.

When several FBGs are glued on Ω adjacent to the defect, as depicted in figure 2, their axial strain will be induced after the excitation of equation (18) and the constraints of equation (17) are imposed. The corresponding strain profiles can

then be obtained from the above elastic boundary problem. For our damage reconstruction, one strategy is to inversely determine the geometry of the defect Γ, including its location, size, and shape, through equations (14)–(18) using the measured strain profiles of the FBGs. Thus, we define two problems:

(a) Direct elastic problem: solving equations (14)–(16) to determine the strain profiles of the FBGs near the known defect with the prescribed geometry and elastic property of the structure as well as the boundary conditions given by equations (17)–(18).
(b) Inverse elastic problem: solving equations (14)–(16) to determine the location and geometry of the unknown defect when the strain profiles of the FBGs glued nearby are measured, with the prescribed geometry and elastic property of the structure as well as the applied boundary conditions given by equations (17)–(18).

3.2. Photo-elastic

Furthermore, after solving the direct elastic problem, one can calculate the reflection intensity spectra of the FBGs through equations (3)–(13). In fact, the combination of equations (3)–(18) constitutes the photo-elastic problem. For our damage reconstruction, another strategy is to determine the location and geometry of the unknown defect, through equations (3)–(18), directly from an inversion of the measured reflection intensity spectra of the FBGs glued nearby. Thus, corresponding to the elastic problems, we also define:

(a) Direct photo-elastic problem: solving equations (3)–(16) to determine the reflection intensity spectra of the FBGs glued near the known defect, with the prescribed geometry and elastic property of the structure as well as the applied boundary conditions given by equations (17) and (18).
(b) Inverse photo-elastic problem: solving equations (3)–(16) to determine the location and geometry of the unknown defect when the reflection intensity spectra of the FBGs glued near the defect are measured, with the prescribed geometry and elastic property of the structure as well as the applied boundary conditions given by equations (17) and (18).

As mentioned above, there are two strategies for dealing with our damage reconstruction. In the first strategy, the profiles of the axial strain of the FBGs could be measured based on an inversion study of their reflection intensity spectra, as presented in section 1. That is to say, we need a two-step inversion process for our damage reconstruction: the reflection intensity spectra of FBGs—strain profiles of gratings—and the location and geometry of a defect. In the second strategy, however, the strain profiles of FBGs play the role of intermediate functions that influence the reflection intensity spectra according to equations (12) and (13), and thus only a one-step inversion study is required, saving much computation time. In fact, the two strategies give almost the same solution, as illustrated in section 5. Hence, the one-step inversion is adopted in our work.

4. Optimization approach for damage reconstruction

In general, directly solving inverse problems is a complex task due to their nonlinearity and the limited measurement information, so they are often transformed to optimization problems and solved in an indirect way. This method is also adopted here for our damage reconstruction.

4.1. Parameterized characterization of damage

We assume that the defect geometry can be adequately characterized by means of a finite number B of scalar parameters, collectively denoted by the B-vector $\mathbf{b} \in R^B$. For a plane void, or a hole, as depicted in figure 3(*a*), the contour Γ of the arbitrary shape could be represented approximately by an equiangular polygon. For this polygon, (r_x, r_y) are the coordinates of its central point in the coordinate system XOY, and $(l_1, l_2, \ldots, l_n)$ is the vector of the corresponding characteristic lengths, i.e. the radii of polygon vertices, where n is the total number of sides or vertices of the polygon. Thus, the void could be characterized by $n + 2$ parameters, and the corresponding parameter vector is $\mathbf{b} = (r_x, r_y, l_1, l_2, \ldots, l_n)$. However, for a plane crack, as depicted in figure 3(*b*), the parameterized characterization is relatively simple, and only a four-parameter vector $\mathbf{b}$ is needed, i.e. $\mathbf{b} = (r_x, r_y, l_c, \theta)$, where (r_x, ry) are the coordinates of the crack center, l_c is half the crack length, and θ is the crack inclination angle.

4.2. Optimization scheme

For a given choice of the parameter vector $\mathbf{b}$ within some admissible set $B \subseteq R^B$ and the prescribed boundary conditions, we first obtain the strain field of the structure and then calculate the reflection intensity spectra of the FBGs from the solution to the direct photo-elastic problem. Therefore, solving the inverse photo-elastic problem amounts to finding values of $\mathbf{b}$ such that the simulated reflection intensity spectra agree with the measured spectra with a certain precision. This can be formulated as the minimization of the objective functional

$$E(\mathbf{b}) = \sum_{j=1}^{M} \int_{\lambda_{jl}}^{\lambda_{ju}} \left[g_j(\lambda) - r_j(\lambda, \varepsilon_j(x, L_j, \mathbf{b}, \phi)) \right]^p \mathrm{d}\lambda, \quad (19)$$

where M is the total number of the FBGs, $g_j(\lambda)$ represents the measured reflection intensity spectrum of the jth FBG, λ_{jl} and λ_{ju} are the lower and upper limits of the spectrum width, respectively, and p is a norm. Moreover, $r_j(\lambda, \varepsilon_j(x, L_j, \mathbf{b}, \phi))$ is the corresponding simulated spectrum with $\varepsilon_j(x, L_j, \mathbf{b}, \phi)$ being the simulated axial strain profile over the length L_j of the grating under the boundary excitation ϕ for an estimation of $\mathbf{b}$.

Discretizing the reflection intensity spectrum by dividing the spectrum width $\lambda_{j2} - \lambda_{j1}$ into N equal zones, the objective functional (19) may be rewritten as

$$E = \sum_{j=1}^{M} \frac{\lambda_{ju} - \lambda_{jl}}{N} \sum_{k=1}^{N} \left[g_j(\lambda(k)) - r_j(\lambda(k), \varepsilon_j(x, L_j, \mathbf{b}, \phi)) \right]^2 \quad (20)$$

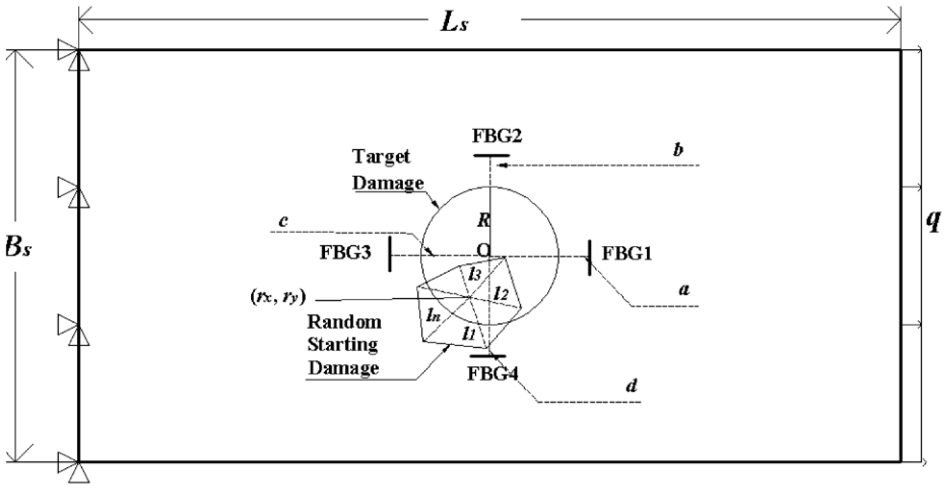

(a)

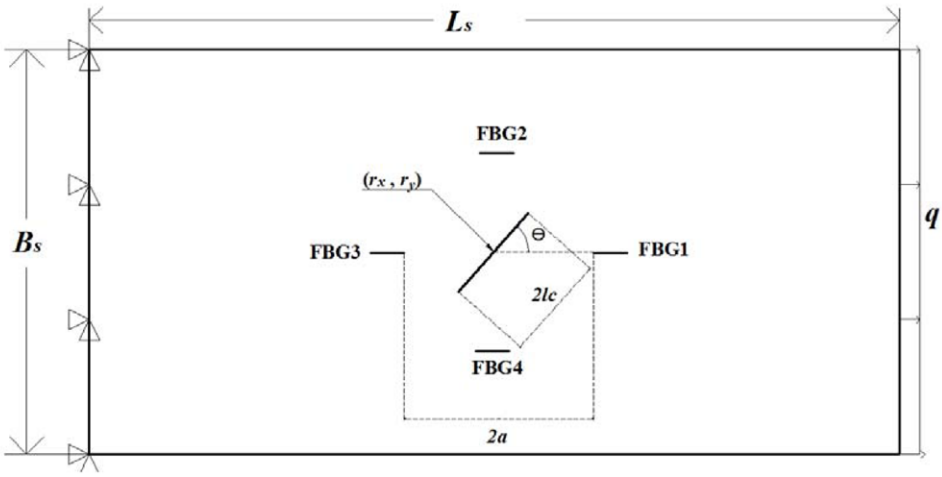

(b)

Figure 3. Parameterized characterization of plane damage: (*a*) void and (*b*) crack.

using $p = 2$. A dimensionless form of equation (20) is given by

$$\overline{E} = \frac{E}{\sum_{j=1}^{M} \frac{\lambda_{ju} - \lambda_{jl}}{N} \sum_{k=1}^{N} \left[g_j(\lambda(k)) \right]^2} . \tag{21}$$

The inverse problem is now reduced to determining the parameter vector **b** by minimizing the objective functional $\overline{E}$. This problem can be solved iteratively based on a suitable optimization algorithm, until $\overline{E}$ is less than a prescribed value δ, i.e.

$$\overline{E} < \delta . \tag{22}$$

Indeed, $\overline{E}$ stands for a dimensionless error functional that is a measure of the distance between the simulated and measured reflection intensity spectra.

In our work, a genetic algorithm (GA) was used as the optimization algorithm to avoid possible convergence to local extreme points. The basic concepts of GAs were developed by Holland [33], who developed a search heuristic that mimics the process of natural evolution. GAs belong to the larger class of evolutionary algorithms (EAs), which generates solutions to optimization problems using the techniques of inheritance, mutation, selection, and crossover [34].

Figure 4 presents the major steps of the GA optimization algorithm for our damage reconstruction. Initially, the GA generates a group of random starting solutions (**b** vectors), and using the finite element and *T*-matrix methods, the strain profiles of the gratings and the corresponding reflection intensity spectra are calculated, respectively, for each **b** vector. Subsequently, these spectra are substituted into equations (20) and (21) to determine their error values, which are also used here as fitness functions in the GA. If the error between the target or measured spectra and the calculated spectra is less than the allowed error δ, the optimization program is terminated. Otherwise, the

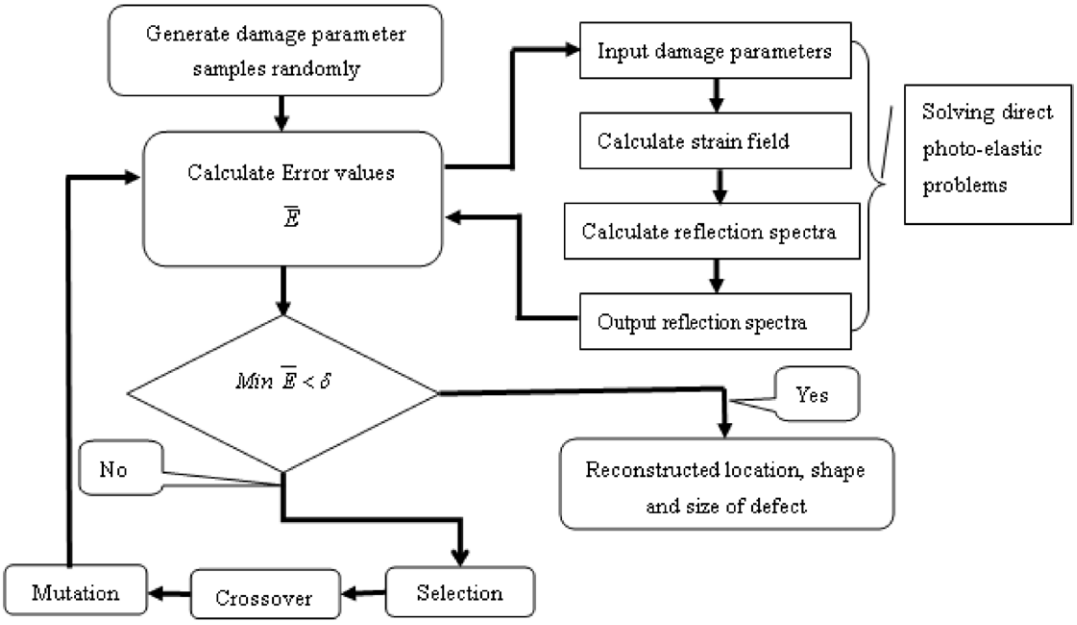

Figure 4. Flow chart of the GA for optimization of damage reconstruction.

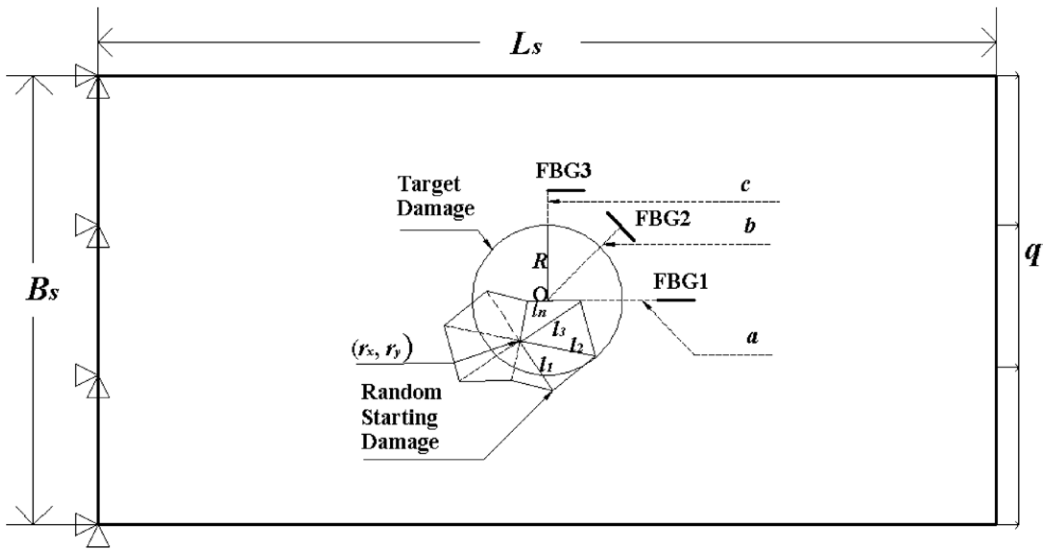

Figure 5. A sample plate with a hole for the damage reconstruction simulation.

selection and crossover operations are performed, followed by the mutation process, which changes one or several values of the components of the **b** vector in the sample strings to other values within the search space, preventing the generation of a local optimal solution. This iterative process is repeated until either equation (22) is satisfied or the specified number of iteration loops has been reached.

5. Numerical proof-of-concept validation

The proof-of-concept validation of our approach was based on a numerical simulation of the damage reconstruction. Effects on the damage identifiability were evaluated pertaining to the details of the deployment of the sensors, including the total number of sensors, distances to the defect, and configuration. The defects considered are plane voids and cracks.

Table 1. Properties of FBGs used for numerical proof-of-concept validation.

Parameter	Value
Modulation amplitude of refractive index Δn	1×10^{-4}
Effective refractive index n_0	1.468
Poisson's ratio ν	0.16
Grating length L (mm)	10
Center wavelength λ_B (nm)	1535.528
Photo-elastic coefficient P_{11}	0.113
Photo-elastic coefficient P_{12}	0.252

5.1. Voids

A plate with a hole in it was selected as the tension sample, as shown in figure 5. The plate was rectangular with length L_s = 260 mm and width B_s = 80 mm. Considering the later

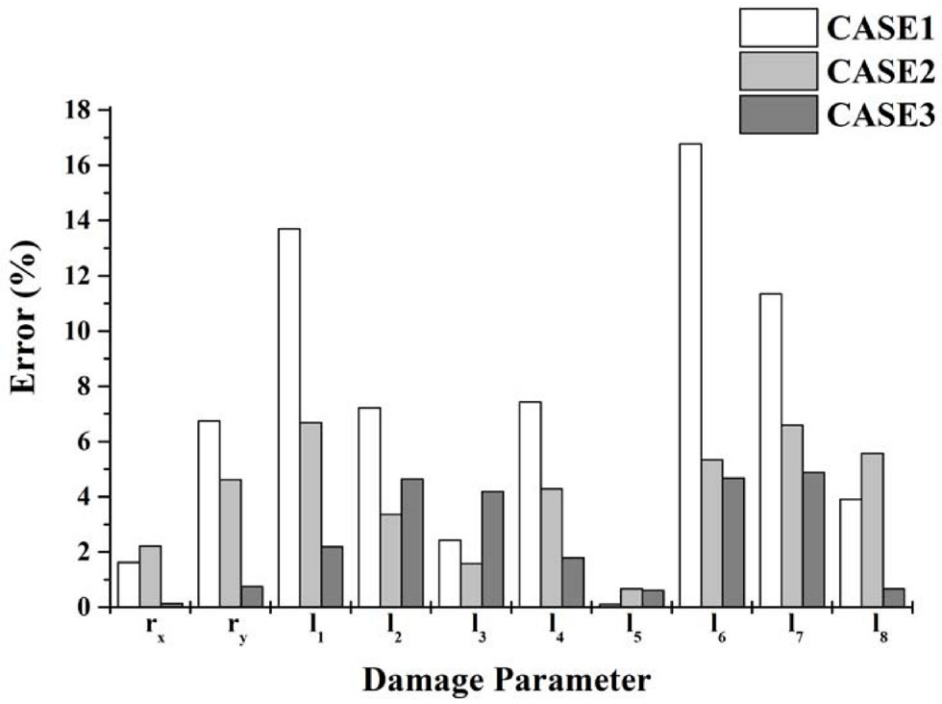

Figure 6. Effect of the total number of the FBGs on the relative errors in the reconstructed damage parameters, compared with the target ones.

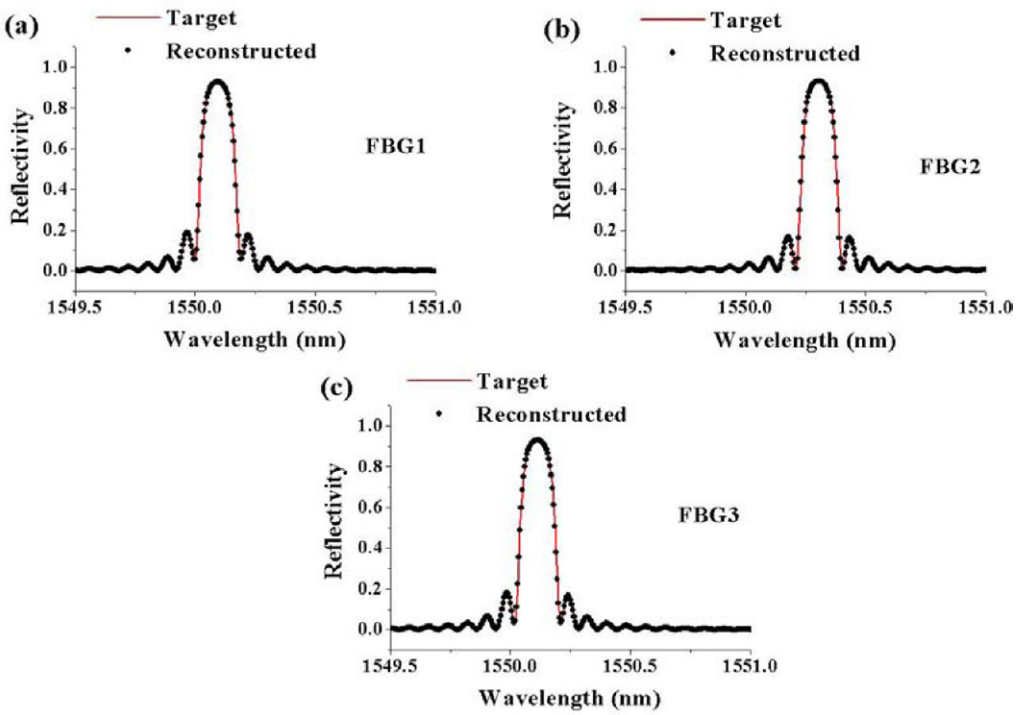

Figure 7. Comparison between the target and reconstructed reflection intensity spectra for the three FBGs for CASE3: (*a*) FBG1, (*b*) FBG2, and (*c*) FBG3.

experimental validation comparison and for the sake of convenience in the damage fabrication, a central circular hole with radius $R = 15$ mm was chosen as the known target damage. This choice did not lead to any loss of generality because the simulation was performed starting with all initial damage parameters selected randomly.

The plate was isotropic with Young's modulus $E = 70$ GPa and Poisson's ratio $\nu = 0.3$. In the simulation, a uniform tensile loading $q = 20$ MPa was imposed on one end of the plate with the other end being fixed. The thickness of the plate t was used as the length unit, and the problem was treated as a plane-stress problem. Three FBGs were deployed near the hole:

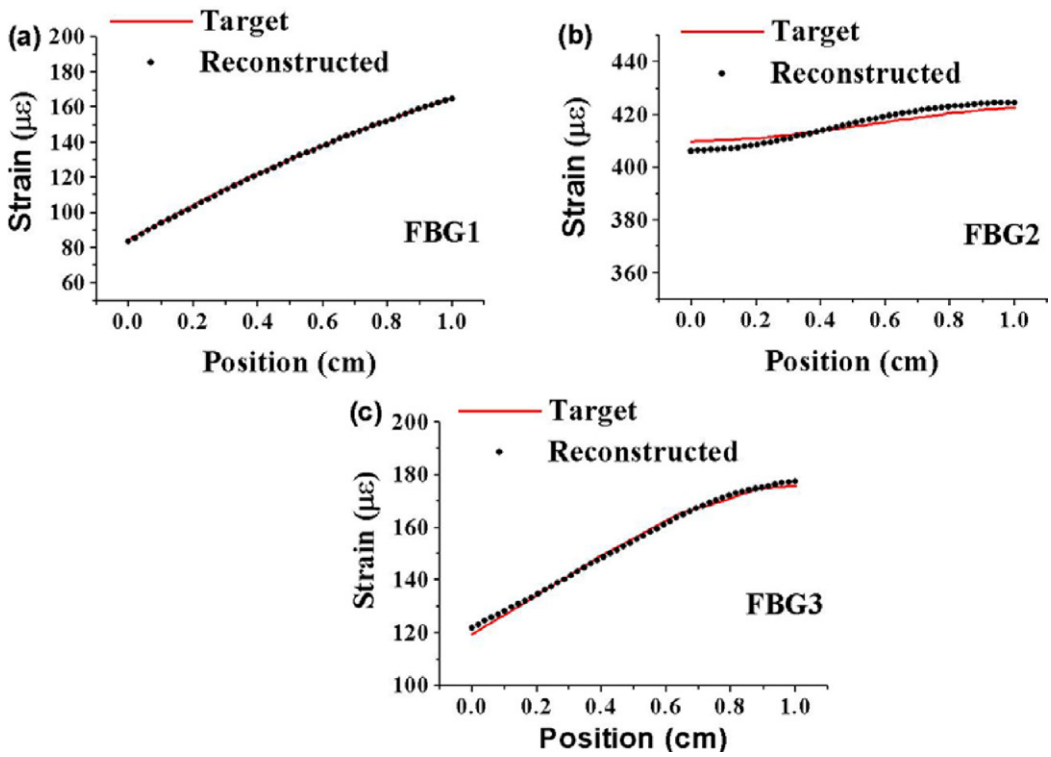

Figure 8. Comparison between the target and reconstructed strain profiles over the gratings of three FBGs in CASE3: (*a*) FBG1, (*b*) FBG2, and (*c*) FBG3.

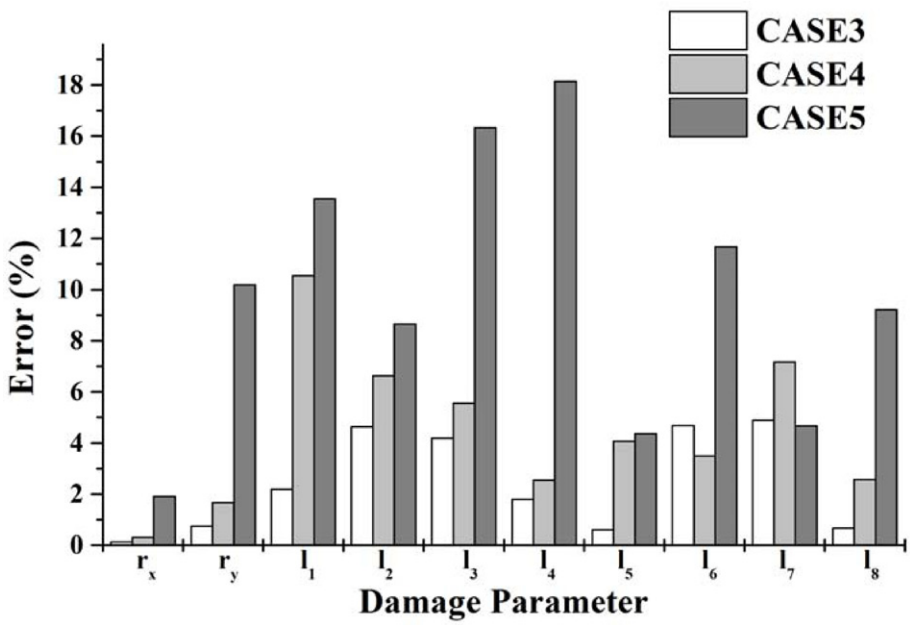

Figure 9. Effect of the sensor to defect distance on the relative errors in the reconstructed damage parameters, compared with the target ones.

FBG1 and FBG3 were in the horizontal direction, and FBG2 was symmetrically vertical to the 45° line. The locations of FBG1, FBG2, and FBG3 are denoted by *a*, *b*, and *c*, respectively, as depicted in figure 5. These are the closest distances between the FBGs and the center of the defect. The FBGs had the same properties with the fixed modulation amplitude of refractive index

$$\Delta n(z) = \Delta n\,. \tag{23}$$

The 'dc' perturbation of refractive index and the index modulation phase were set as $\delta n(z) = 0$ and $\phi(z) = 0$, respectively. All of the FBG parameters are listed in table 1.

Because the target hole is centrosymmetric, we first made the damage reconstruction with centrosymmetric equiangular

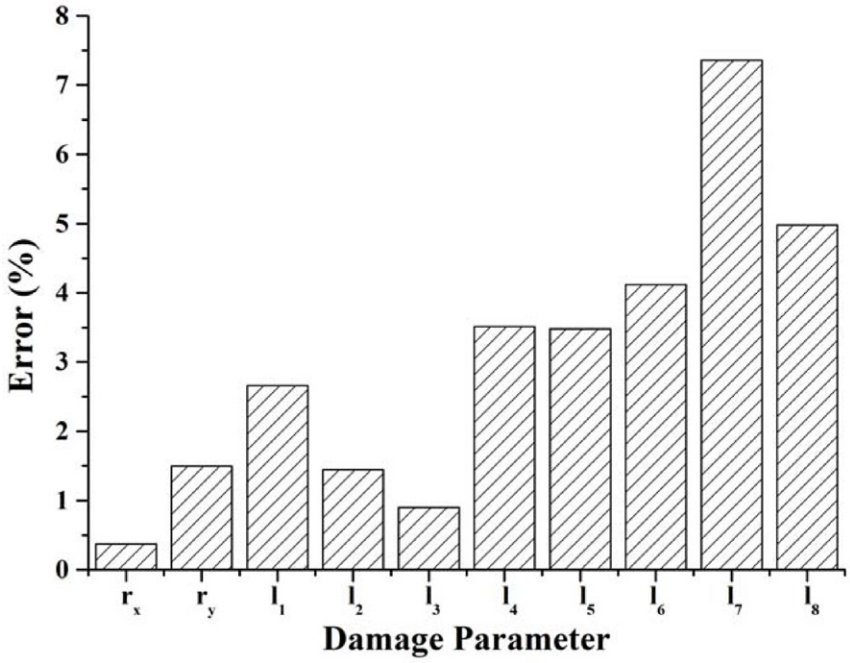

Figure 10. Relative errors of the reconstructed damage parameters compared with the target damage parameters.

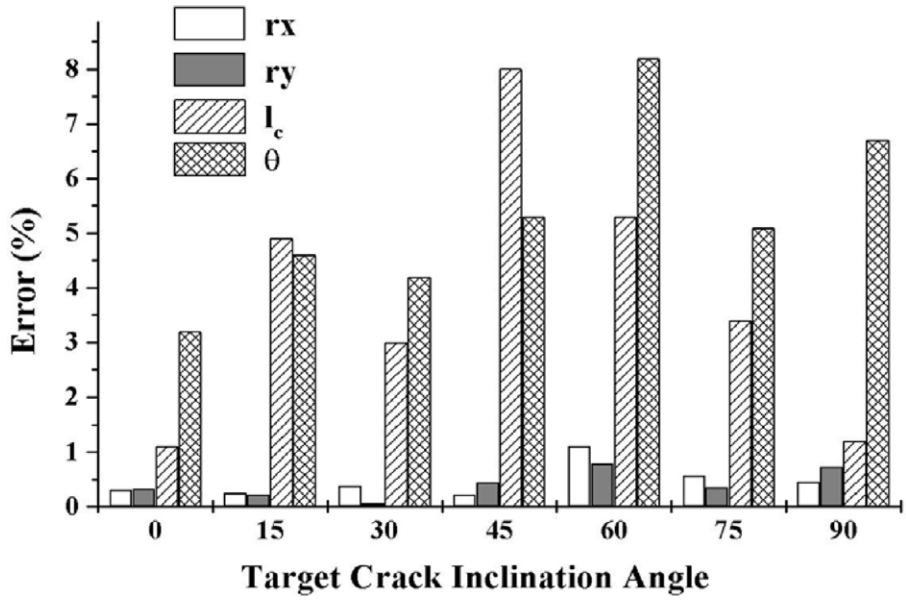

Figure 11. Dependence of the relative errors of the reconstructed damage parameters on the target crack inclination angle compared with the target ones.

polygons to approximate the target defect, for the sake of reducing the computational work, and then we repeated the calculation with arbitrary equiangular polygons. The initial damage parameters $\mathbf{b} = (r_x, r_y, l_1, l_2, \ldots, l_n)$ of the centrosymmetric equiangular polygon were randomly selected as shown in figure 5.

5.1.1. Damage reconstruction with centrosymmetric equiangular polygons.

Effect of the total number of the FBGs. Three cases were considered in the simulation. In CASE1, only FBG1 was used, both FBG1 and FBG3 were used in CASE2, and all three sensors, FBG1, FBG2, and FBG3, were used in CASE3. The dimensionless distances of these sensors were the same and were set as $a/R = b/R = c/R = 5/3$. Ten damage parameters were selected in all three cases. The selected damage parameters were the two coordinate parameters of the polygon center, (r_x, r_y), and eight centrosymmetric characteristic length parameters, $(l_1, l_2, \cdots, l_8)$, as depicted in figure 5. The target reflection-intensity spectra were calculated through solving the direct photo-elastic problem for the prescribed target damage.

Figure 6 indicates the relative errors between the reconstructed and target damage parameters for CASE1, CASE2,

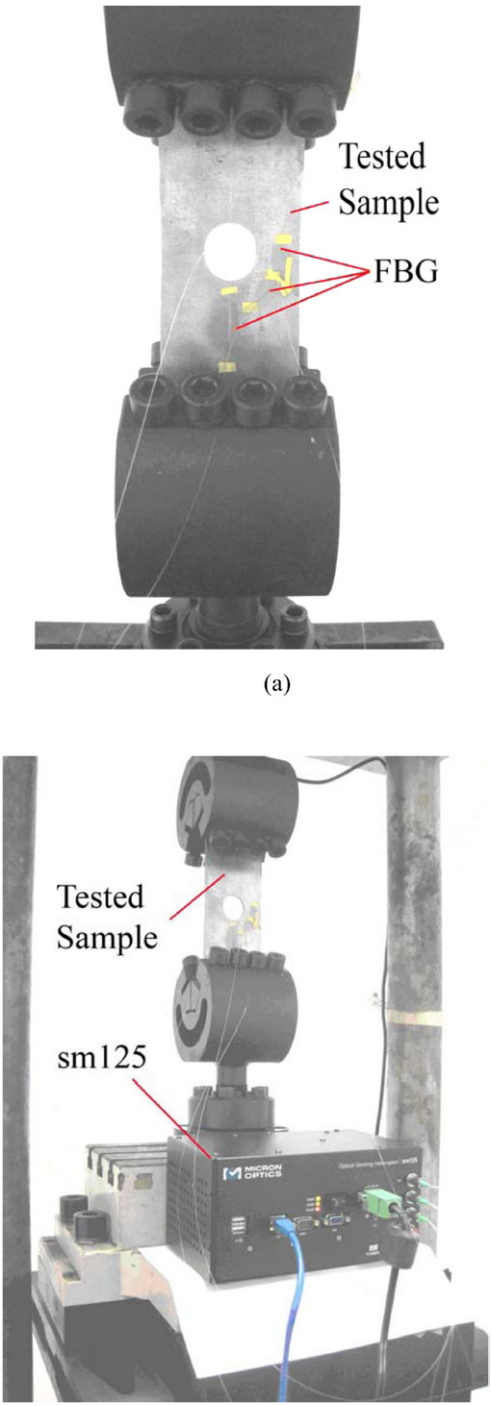

Figure 12. Experimental setup for validation: (*a*) tested plate and (*b*) experimental setup.

and CASE3. In general, it can be seen that the damage identifiability, which is implied by the relative errors, increases with increasing numbers of FBGs. The maximum errors are 16.77%, 6.59%, and 4.89% for CASE1, CASE2, and CASE3, corresponding to l_6, l_7, and l_7, respectively. The results demonstrate that the increase in measured information about the reflection intensity spectra of the FBGs leads to higher damage identifiability, as expected. It can also be noted that although the initial characteristic length parameters $(l_1, l_2, \cdots, l_8)$ were selected randomly, they tended to converge to the common target value R, within acceptable precision. Using only three FBGs in this simulation, we could reach a high identifiability, with an error of less than 5%. Even though single FBG1 is used, the error is not more than 17%, for this symmetrical case. That is owing to the line-wise truly distributed strain information measured from the FBG sensor. It includes the information of multiple orders of strain gradients, in contrast to the conventional sensor, and so relates the defect more closely.

Note that there is some randomness in the distribution of the relative parameters with respect to different damage parameters. That is the inherency of GA. It generates solutions vibrating near the optimal one but cannot converge to it, unless followed by another deterministic optimization algorithm, such as gradient algorithm. Besides, the orientation with respect to the loading direction and the sensor to defect side distance also affect the distribution of relative errors, corresponding to different damage parameters.

Figures 7(*a*)–(*c*) represent a comparison between the target (calculated from the target defect) and reconstructed reflection intensity spectra of the three FBGs in CASE3, corresponding to figure 6, showing a good convergence of the simulated spectra to the target spectra. Figures 8(*a*)–(*c*) display the corresponding reconstructed strain profiles over the gratings of the three FBGs, compared with the target strain profiles (calculated from the target defect). A good coincidence is also noted in figure 8, which gives an indirect illustration that the damage identifiability of the one-step (reflection-intensity-spectrum-based) and two-step (strain-based) inversions are approximately equivalent in our damage reconstruction. It is worthy noting that although the distortion of the reflection spectra in figures 7(*a*)–(*c*) is not obvious, the remarkably nonuniform strain distributions are inverted with a good precision, as shown in figures 8(*a*)–(*c*). This sensibility of the reflection spectrum to strain gradient plays a crucial role in the present approach to gain high damage identifiability.

Effect of the FBG distances to the defect. In this simulation, the deployment configuration of the FBG sensors corresponds to CASE3 in the above simulation. Three different sensor distances to the defect center were selected. In addition to CASE3 with $a/R = b/R = c/R = 5/3$, we selected CASE4 as $a/R = b/R = c/R = 2$ and CASE5 as $a/R = b/R = c/R = 7/3$. The other simulation input data were the same as those of CASE3, and again ten damage parameters were selected.

Figure 9 shows the relative errors between the reconstructed and target damage parameters for CASE3, CASE4, and CASE5. Note that, in general, the damage identifiability decreases with increasing sensor distance to the defect center. The maximum errors are 4.89%, 10.55%, and 18.14%, corresponding to l_7, l_1, and l_4 for CASE3, CASE4, and CASE5, respectively. The result could be readily understood from elasticity mechanics because the remarkable strain gradient comes mainly from the disturbed strain field around a defect, relative to the undisturbed strain field of the intact structure, which

Table 2. Properties of FBGs used for experimental validation (void).

Parameter	Sensors		
	FBG1	FBG2	FBG3
Modulation mode of refractive index	Gaussian	Gaussian	Gaussian
Central modulation amplitude of refractive index Δn	1.53×10^{-4}	1.75×10^{-4}	1.87×10^{-4}
Apodization factor a_G	7.51	11.32	11.57
Effective refractive index n_0	1.369	1.519	1.355
Poisson's ratio ν	0.17	0.17	0.17
Grating length L (mm)	10.2	10.9	11.0
Center wavelength λ_B (nm)	1535.660	1535.660	1535.620
Photo-elastic coefficient P_{11}	0.113	0.113	0.113
Photo-elastic coefficient P_{12}	0.252	0.252	0.252

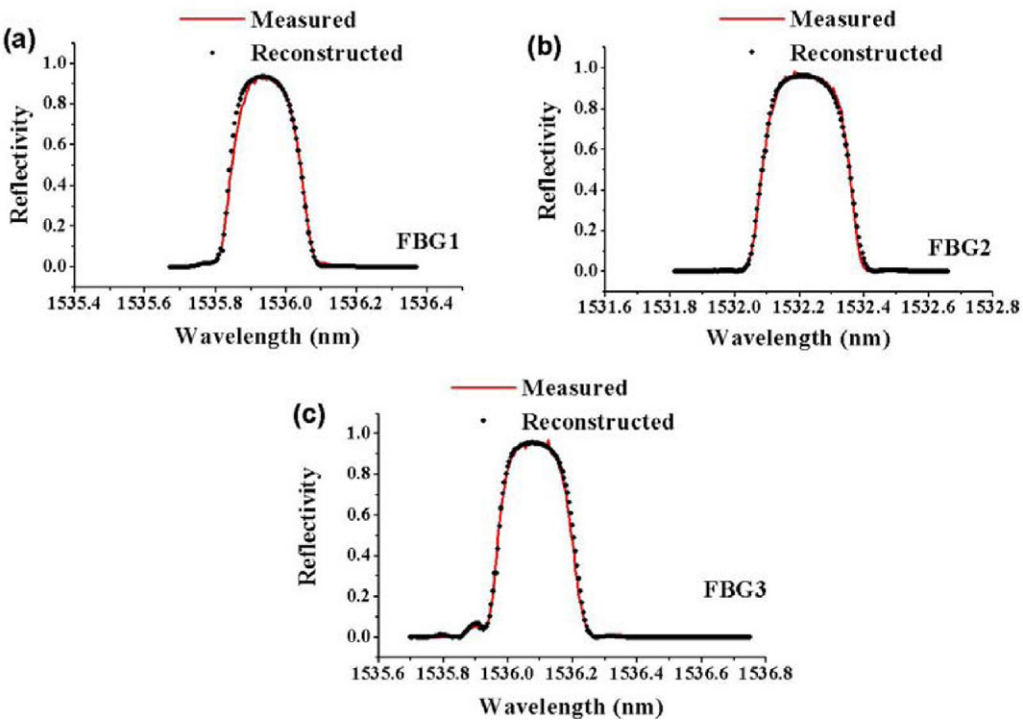

Figure 13. Comparison between the measured and reconstructed reflection intensity spectra for (*a*) FBG1, (*b*) FBG2, and (*c*) FBG3, deployed in the sample with a hole.

tends to disappear with increasing distance to the defect. In the present case of plane problem, for instance, the disturbed strain field decays with $(r/R)^{-2}$, where r is the the distance to the defect center and R is the defect size, i.e. the radius of the circular void. Therefore, our approach is a local one and its applicable premise is that the remarkable disturbed strain field information must be captured by FBG sensors. For the given defect size, the damage identifiability decreases with the increasing sensor to defect distance, as shown by figure 9. While, if the defect is close to the sensor, it can be reconstructed better even when its size is small. That is to say, earlier damage may be constructed by the present approach, as long as its relative distance to the FBG sensor is small. Thus, the present approach is applicable to monitor the evolution of damage to hotspots of structures, which are known important sites of stress concentration where damage appears preferentially.

5.1.2. Damage reconstruction with arbitrary equiangular polygons. The simulation was extended by using arbitrary equiangular polygons instead of centrosymmetric polygons. The sample as well as the loading used for the numerical proof-of-concept validation is given in figure 3(*a*). This sample is the same as the sample shown in figure 5, except that four FBG sensors were deployed centrosymmetrically about the defect with the same distance: $a/R = b/R = c/R = d/R = 2$ (corresponding to CASE4 in section 5.1.1). The total number of damage parameters was still ten, and the other parameters used for simulation were the same as those in section 5.1.1.

Figure 10 presents the relative errors between the reconstructed and target damage parameters. The maximum error is 7.36%, corresponding to l_7, illustrating that good damage identifiability is achievable in our approach using general equiangular polygons to approximate the target void.

5.2. Cracks

The dimension and loading of the sample used for the simulation of the reconstruction of a crack are shown in figure 3(*b*),

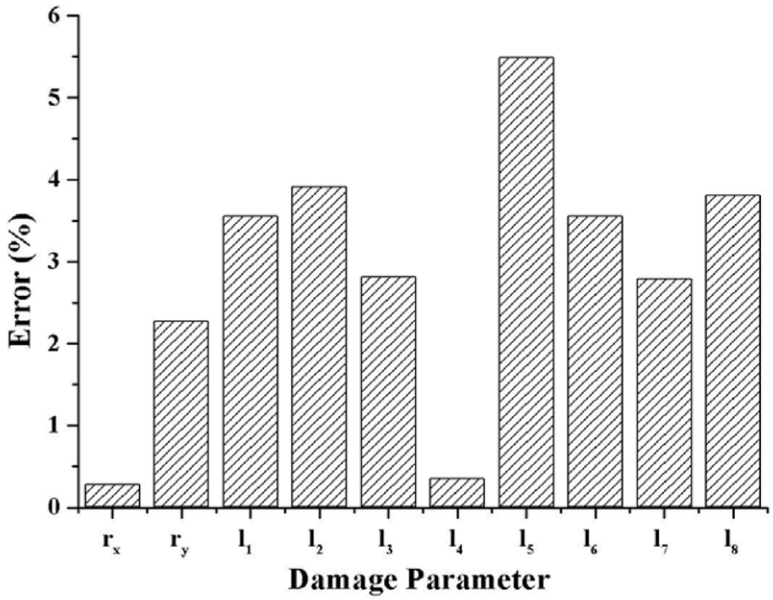

(a)

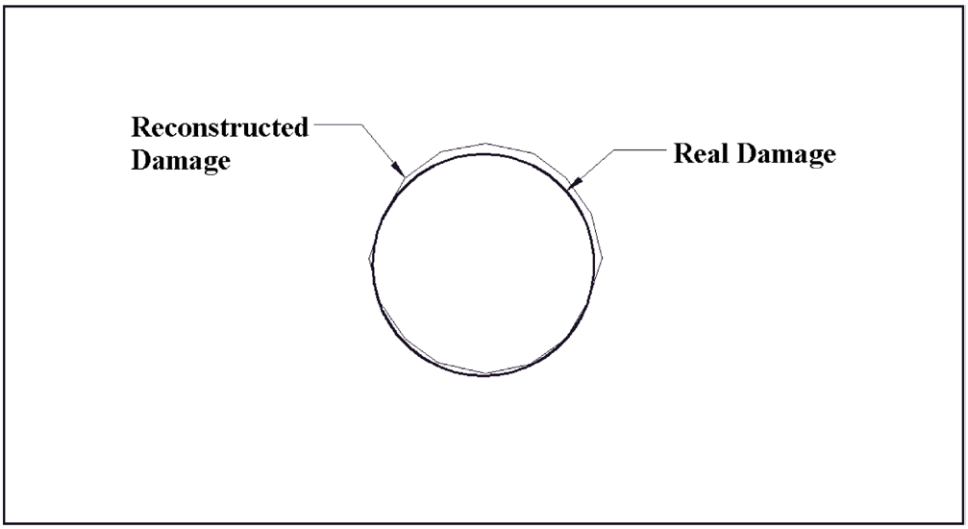

(b)

Figure 14. Comparison between the reconstructed damage and real damage: (*a*) relative errors of the damage parameters and (*b*) contour.

which is the same as figure 3(*a*) except that the target void was replaced by a target crack. Moreover, the material of the sample was the same, and the same four FBG sensors were deployed centrosymmetrically about the center of the crack, with a dimensionless distance $a/l_c = 2$. The total number of damage parameters was four, and their initial values were selected randomly.

Figure 11 shows the variation of the relative errors of the reconstructed damage parameters with the target crack inclination angle compared with the target damage parameters. In the simulation, the position of the target crack was kept unchanged, and half the crack length was fixed at 10 mm. Better identifiability is achieved near the 0° and 90° crack inclination angles, while bigger errors occur near the 45–60° crack inclination angles. This difference is due to the fact that sensors are farther from the crack-tip field in the latter case. However, all relative errors are within 9%, showing a satisfactory crack reconstruction based on our approach.

The above numerical proof-of-concept validation demonstrates that although the complementary information (from FBGs) about the strain field of the structure is limited, the nearby defect could be reconstructed with a high identifiability based on our approach. It effectively monitors the damage evolution in the hotspots of structures, as long as the

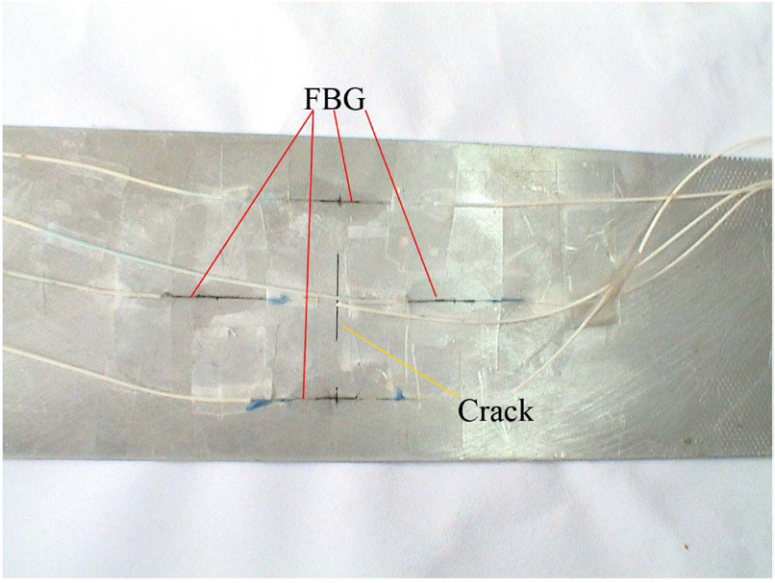

(a)

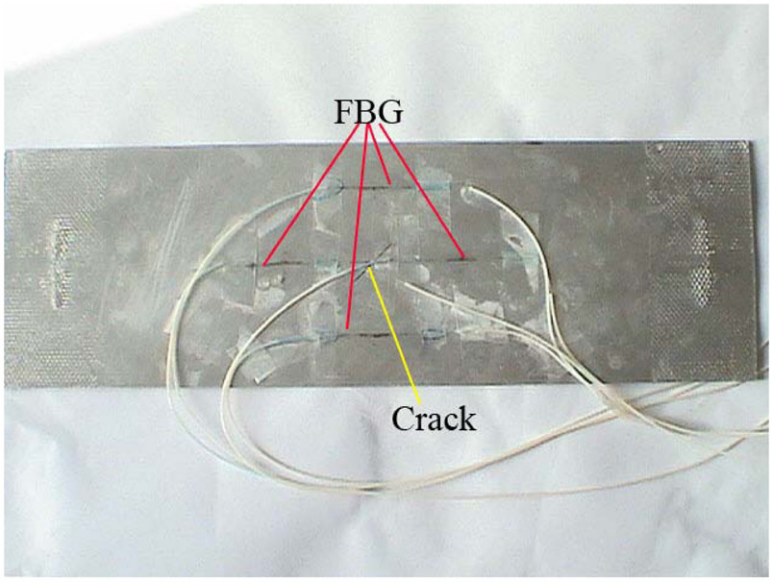

(b)

Figure 15. Tested cracked plate samples: (*a*) $\theta = 90°$ and (*b*) $\theta = 45°$.

total number of sensors is suitable and the sensors are not located too far from the defect, depending on its size.

6. Experimental validation

To readily understand our methodology, plates with holes and cracks like those used in the numerical simulation were selected as structural samples for experimental validation. Note, however, that the application of this method is not limited to these structures.

6.1. Sample plate with holes

The tested sample plate with a hole as well as the three FBGs deployed around the defect, corresponding to CASE3 in section 5.1.1, was photographed (see figure 12(*a*)). The sample was made of steel with Young's modulus $E = 200$ GPa and Poisson's ratio $\nu = 0.3$. The sample was 190 mm long (L_s), 80 mm wide (B_s) and 3 mm thick (t). A hole was prefabricated, with radius $R = 15$ mm, as a known target defect.

To install the FBG sensors, we polished the specimen surface firstly using abrasive paper with a grain size of 800 # and then cleaned it using alcohol. When the surface was dry, we positioned the FBG and pasted loosely the cabling optical fibers outside the ends of the grating sections onto the specimen with adhesive tape to immobilize the sensor and fiber. Finally, we glued uniformly the grating sections onto the specimen surface using liquid cyanoacrylate adhesive (502). In addition, before the test, the free reflection spectra of the FBGs under

Table 3. Properties of FBGs used for experimental validation and deployed in the cracked sample with $\theta = 90°$.

Parameter	Sensors			
	FBG1	FBG2	FBG3	FBG4
Modulation mode of refractive index	Gaussian	Gaussian	Gaussian	Gaussian
Central modulation amplitude of refractive index Δn	1.91×10^{-4}	2.0×10^{-4}	2.0×10^{-4}	2.0×10^{-4}
Apodization factor a_G	11.0	17.36	11.0	15.56
Effective refractive index n_0	1.370	1.512	1.420	1.406
Poisson's ratio ν	0.17	0.17	0.17	0.17
Grating length L (mm)	9.3	10.7	9.0	10.3
Center wavelength λ_B (nm)	1550.430	1550.070	1550.400	1550.072
Photo-elastic coefficient P_{11}	0.113	0.113	0.113	0.113
Photo-elastic coefficient P_{12}	0.252	0.252	0.252	0.252

Table 4. Properties of FBGs used for experimental validation and deployed in the cracked sample with $\theta = 45°$.

Parameter	Sensors			
	FBG1	FBG2	FBG3	FBG3
Modulation mode of refractive index	Gaussian	Gaussian	Gaussian	Gaussian
Central modulation amplitude of refractive index Δn	1.85×10^{-4}	1.98×10^{-4}	1.96×10^{-4}	1.80×10^{-4}
Apodization factor a_G	15.46	13.67	15.88	9.74
Effective refractive index n_0	1.490	1.46	1.445	1.469
Poisson's ratio ν	0.17	0.17	0.17	0.17
Grating length L (mm)	10.6	10.5	10.4	11.6
Center wavelength λ_B (nm)	1551.185	1550.230	1550.230	1550.340
Photo-elastic coefficient P_{11}	0.113	0.113	0.113	0.113
Photo-elastic coefficient P_{12}	0.252	0.252	0.252	0.252

unloading state were measured by an optical sensing interrogator (sm125, Micron Optics Inc.) with high wavelength accuracy (error less than 1 pm). The free reflection spectra were then used for the inversion of the property parameters of FBGs based on the T-matrix. They are listed in table 2. These FBGs had Gaussian-distributed modulation amplitudes of the refractive index:

$$\Delta n(z) = \Delta n \exp\{-a_G[(z - L/2)/L]^2\}, \tag{24}$$

where Δn is the central index modulation amplitude, and a_G is the width of the Gaussian depth (i.e. the apodization factor). In addition, the 'dc' perturbation of refractive index $\delta n(z) = 0$, and the index modulation phase $\phi(z) = 0$. The dimensionless distance of the FBGs to the center of the hole was $a/R = b/R = c/R = 5/3$.

As shown in figure 12(*b*), a static load was imposed by a material testing machine (PLG-100) with a loading accuracy of 0.1%. At the same time, the reflection intensity spectra of the FBG sensors were recorded by sm125. After the test, the damage reconstruction was carried out based on our approach using centrosymmetric equiangular polygons.

Figure 13 shows a comparison between the measured and reconstructed reflection intensity spectra for the three FBGs, with loading q = 20 MPa, indicating a good agreement between them. The corresponding reconstructed damage parameters and defect contour are indicated in figures 14(*a*) and (*b*), compared with the real ones. The maximum relative error is 5.49%, corresponding to l_5, illustrating that high damage identifiability is achievable through our approach.

6.2. Cracked plate sample

Figures 15(*a*) and (*b*) show the two tested cracked plate samples. Their material and dimension are the same, but the crack inclination angles are 90° and 45°, respectively. The samples were made of aluminum with Young's modulus E = 70 GPa and Poisson's ratio ν = 0.3. The samples were 260 mm long, 80 mm wide, and 2 mm thick. A crack was prefabricated for each sample, with a fixed half-crack length l_c = 15 mm, as the known target defect. Around the crack, four FBGs were deployed centrosymmetrically in the horizontal direction for each sample at a fixed distance a = 25 mm. They were installed in the same way as the sample plate with holes presented above. The grating properties of the FBG sensors were also inverted based on T-matrix that are listed in tables 3 and 4, respectively, for the samples shown in figures 15(*a*) and (*b*).

Figures 16(*a*)–(*c*) show the results of the experimentally reconstructed damage parameters compared with the target parameters for the two samples subjected to the loading q = 20 MPa. From figure 16(*a*), it is noted that the maximum relative error is 6.1%, corresponding to the damage parameter θ for the sample with $\theta = 90°$. This result is somewhat different from the tendency of the simulated one as indicated in figure 11, where the maximum error occurs near $\theta = 45°$. This difference might be due to the test error. Figures 16(*b*) and (*c*) indicate

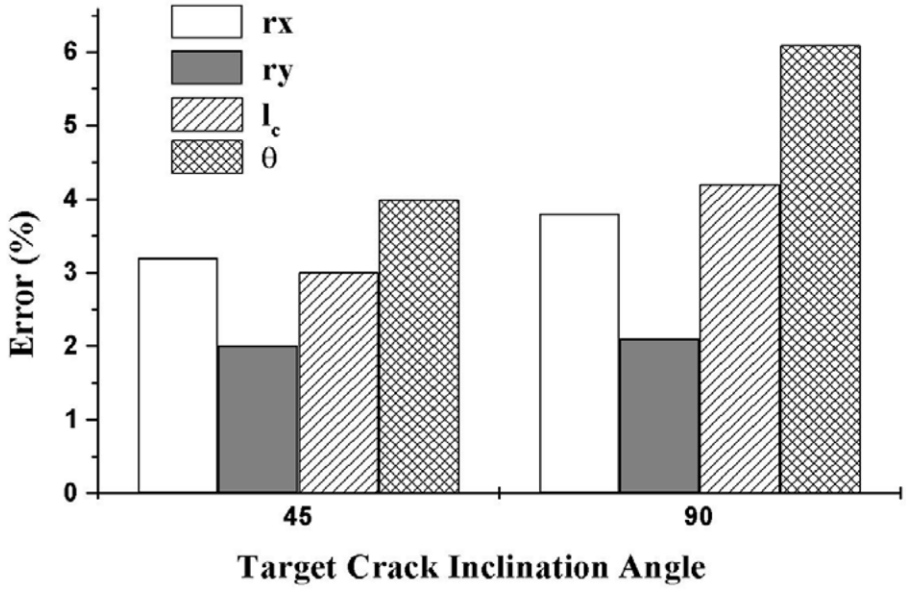

(a)

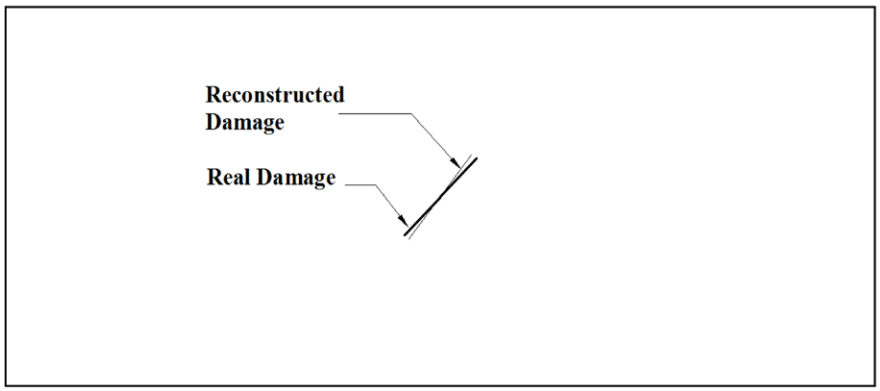

(b)

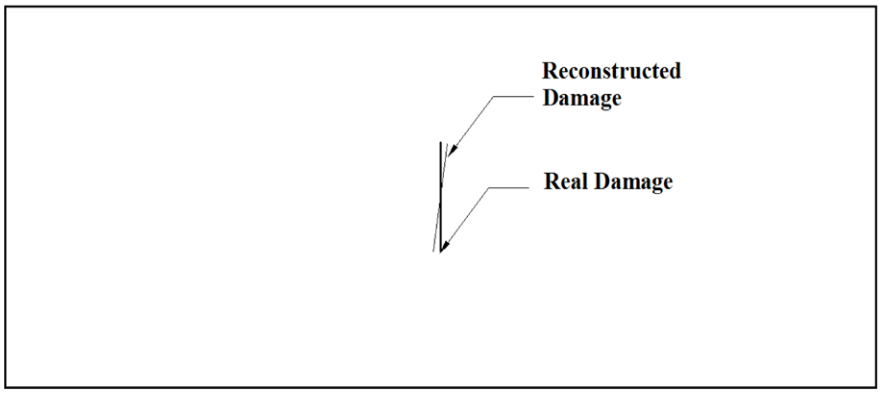

(c)

Figure 16. Relative errors of the experimentally reconstructed damage parameters, compared with the target damage parameters, and the corresponding defect geometries for the samples cracked at $\theta = 45°$ and $\theta = 90°$: (*a*) relative errors of the damage parameters, (*b*) contour, $\theta = 45°$, and (*c*) contour, $\theta = 90°$.

comparisons between the simulated and real defect contours, showing the damage imaging capability. Figures 17(*a*)–(*d*) and 18(*a*)–(*d*) depict the comparisons between the reconstructed reflection intensity spectra and measured spectra for the four FBGs, deployed in the two samples, respectively. There is a good agreement between the simulated and measured spectra.

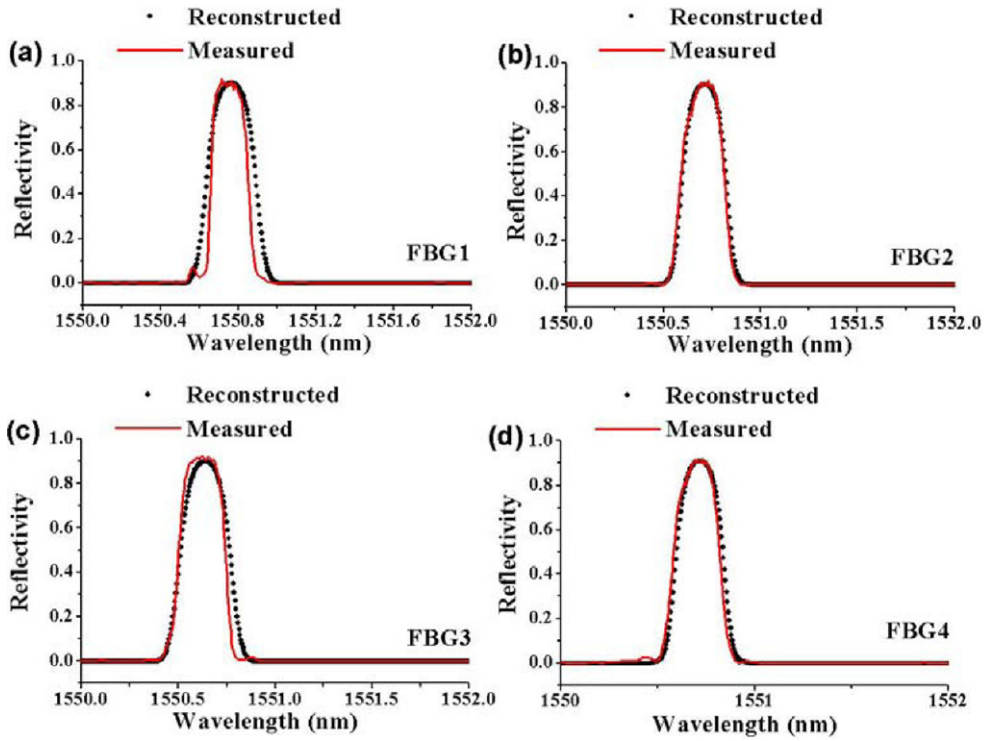

Figure 17. Comparison between the measured and reconstructed reflection intensity spectra for (*a*) FBG1, (*b*) FBG2, (*c*) FBG3, and (*d*) FBG4, deployed in the sample cracked at $\theta = 90°$.

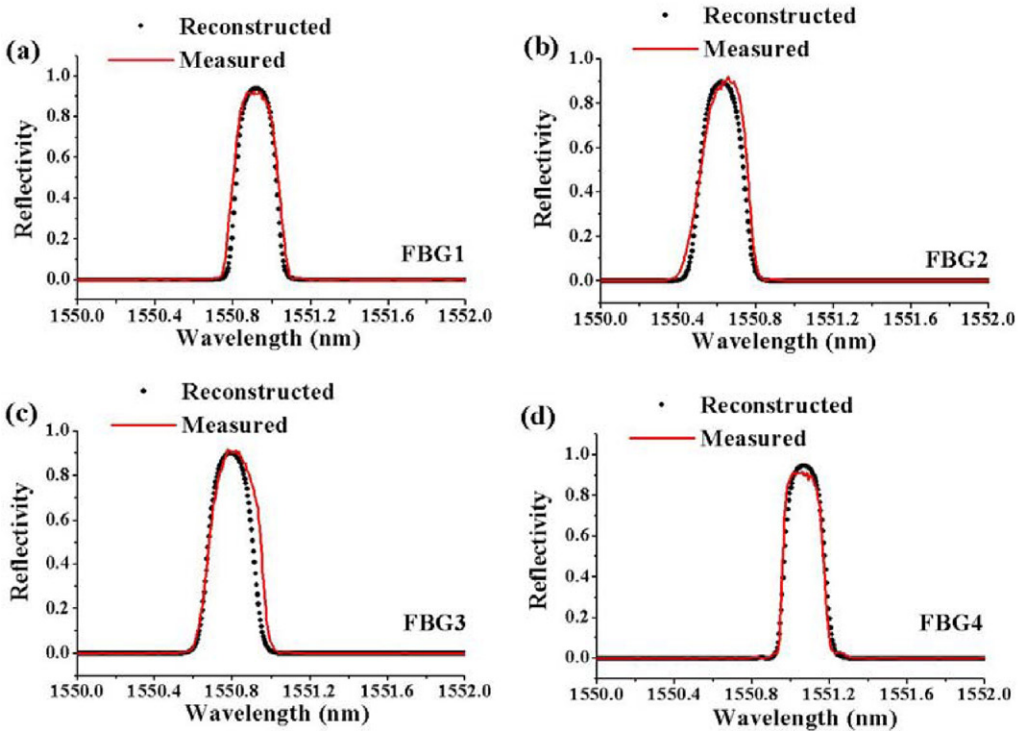

Figure 18. Comparison between the measured and reconstructed reflection intensity spectra for (*a*) FBG1, (*b*) FBG2, (*c*) FBG3, and (*d*) FBG4, deployed in the sample cracked at $\theta = 45°$.

All the experimental results presented above illustrate that satisfactory damage identifiability is achievable, which, together with the theoretical simulation, validates our approach for reconstructing the damage in the planar cases.

7. Conclusion

An optimization approach for damage reconstruction based on the reflection intensity spectra of FBGs has been developed.

Our approach extends FBG-based strain profile reconstruction to damage reconstruction. It incorporates the finite element and *T*-matrix methods for the direct photo-elastic problem and the GA for the corresponding inverse problem. Both the numerical and experimental results show that, by using several FBG sensors, our method is capable of reconstructing the location, size, and shape of the defect in structural hotspots within practically permitted errors. Indeed, it provides us with a photo-elastic method to devise an automatic and remote damage-imaging technique, thus realizing *in-situ* and on-time inspection of structural damage and enhancing the damage identification of SHM. Therefore, our approach enriches FBG-based sensing technology and its application to engineering.

The study presented in the current work was preliminary. It needs to be extended from 2D planar defects to 3D defects. The latter work involves more damage parameters and more complex elastic boundary value problems, so that the reduction of computational complexity is a crucial issue. This work is under way and the corresponding results will be reported later. In addition, the disturbance arising from structural vibration and noise is a very important issue to address in practical application. Since the present damage reconstruction is a static approach, it is required to develop data processing technology to deal with this issue in order to extract the static reflection spectra of FBGs from the time series of the measured reflection spectra.

Acknowledgments

The authors appreciate the support for this work from the High Scientific and Technical Plan, Ministry of Sciences and Technology of China (grant No. 2008AA09Z312) and from the Instrument Research and Development Project, Chinese Academy of Sciences (grant No. 025).

References

[1] Othonos A 1997 Fiber Bragg gratings *Rev. Sci. Instrum.* **68** 4309–41

[2] Todd M D, Nichols J M, Trickey T, Seaver M, Nichols C J and Virgin L N 2007 Bragg grating-based fibre optic sensors in structural health monitoring *Phil. Trans. R. Soc.* A **365** 317–43

[3] Majumder M, Gangopadhyay T K, Chakraborty, A K, Dasgupta K and Bhattacharya D K 2008 Fibre Bragg gratings in structural health monitoring—present status and applications *Sensors Actuators* A **147** 150–64

[4] LeBlanc M, Huang S Y, Ohn M M, Measures R M, Guemes A and Othonos A 1996 Distributed strain measurement based on a fiber Bragg grating and its reflection spectrum analysis *Opt. Lett.* **21** 1405–7

[5] Casagrande F, Crespi P, Grassi A M, Lulli A, Kenny R P and Whelan M P 2002 From the reflected spectrum to the properties of a fiber Bragg grating: a genetic algorithm approach with application to distributed strain sensing *Appl. Opt.* **41** 5238–44

[6] Shi C Z, Zeng N, Zhang M, Liao Y B and Lai S R 2003 Adaptive simulated annealing algorithm for the fiber Bragg grating distributed strain sensing *Opt. Commun.* **226** 167–73

[7] Cheng H C and Lo Y L 2004 Arbitrary strain distribution measurement using a genetic algorithm approach and two fiber Bragg grating intensity spectra *Opt. Commun.* **239** 323–32

[8] Shao J Y and Huang G J 2006 Distributed strain sensing based on fiber Bragg gratings *Nucl. Power Eng*. **27** (suppl.) 279–81 (in Chinese)

[9] Zhang R, Zheng S and Xia Y 2008 Strain profile reconstruction of fiber Bragg grating with gradient using chaos genetic algorithm and modified transfer matrix formulation *Opt. Commun.* **281** 3476–85

[10] Zou H, Liang D, Zeng J and Feng L 2012 Quantum-behaved particle swarm optimization algorithm for the reconstruction of fiber Bragg grating sensor strain profiles *Opt. Commun.* **285** 539–45

[11] Huang S Y, Ohn M M and Measures R M 1996 Phase-based Bragg intra grating distributed strain sensor *Appl. Opt.* **35** 1135–42

[12] Ohn M M, Huang S Y, Measures R M and Chwang J 1997 Arbitrary strain profile measurement within fibre gratings using interferometric Fourier transform technique *Electron. Lett.* **33** 1242–3

[13] Azana J, Muriel M A, Chen L R and Smith P W E 2001 Fiber Bragg grating period reconstruction using time-frequency signal analysis and application to distributed sensing *J. Lightwave Technol.* **19** 646–54

[14] Peters K, Studer M, Botsis J, Iocco A, Limberger H and Salathe R 2001 Embedded optical fiber Bragg grating sensor in a nonuniform strain field: measurements and simulations *Exp. Mech.* **41** 19–28

[15] Okabe Y, Yashiro S, Kosaka T and Takeda N 2000 Detection of transverse cracks in CFRP composites using embedded fiber Bragg grating sensors *Smart Mater. Struct.* **9** 832–8

[16] Takeda S, Okabe Y and Takeda N 2002 Delamination detection in CFRP laminates with embedded small-diameter fiber Bragg grating sensors *Composites* A **33** 971–80

[17] Yashiro S, Takeda N, Okabe T and Sekine H 2005 A new approach to predicting multiple damage states in composite laminates with embedded FBG sensors *Compos. Sci. Technol.* **65** 659–67

[18] Okabe Y, Tsuji R and Takeda N 2004 Application of chirped fiber Bragg grating sensors for identification of crack locations in composites *Composites* A **35** 59–65

[19] Yashiro S, Okabe T, Toyama N and Takeda N 2007 Monitoring damage in holed CFRP laminates using embedded chirped FBG sensors *Int. J. Solids Struct.* **44** 603–13

[20] Ussorio M, Wang H, Ogin S L, Thorne A M, Reed G T, Tjin S C and Suresh R 2006 Modifications to FBG sensor spectra due to matrix cracking in a GFRP composite *Constr. Build. Mater.* **20** 111–8

[21] Takeda N, Yashiro S and Okabe T 2006 Estimation of the damage patterns in notched laminates with embedded FBG sensors *Compos. Sci. Technol.* **66** 684–93

[22] Yashiro S, Okabe T and Takeda N 2007 Damage identification in a holed CFRP laminate using a chirped fiber Bragg grating sensor *Compos. Sci. Technol.* **67** 286–9

[23] Schmerr L W 1998 *Fundamentals of Ultrasonic Nondestructive Evaluation—A Modeling Approach* (New York: Plenum)

[24] Schmerr L W and Song S J 2007 *Ultrasonic Nondestructive Evaluation Systems—Models and Measurements* (New York: Springer)

[25] Colton D and Kress R 1992 *Inverse Acoustic and Electromagnetic Scattering Theory* (Berlin: Springer)

[26] Langenberg K J, Brandfass M, Hannemann R, Kostka J, Marklein R, Mayer K and Pitsch A 2000 Inverse scattering with acoustic, electromagnetic, and elastic waves as applied in nondestructive evaluation *Wavefield Inversion* ed A Wirgin (Berlin: Springer) pp 59–118

[27] Forster E 1985 *Equipment for Diagnostic Radiography* (Lancaster: MTP Press)

[28] Ghosh J K, Panakkal J P, Chandrasekharan K N and Roy P R 1985 A combined X-radiography-gamma-autoradiography (XGAR) technique for characterisation of welded nuclear fuel pins *11th World Conf. on Nondestructive Testing* (*Las Vegas, Nevada*) vol 2 pp 174–80

[29] Jata K V, Knopp J S, Aldrin J C, Medina E A and Lindgren E A 2006 Transitioning from NDE inspection to online structural health monitoring–issues and challenges *Proc. 3rd European Workshop on Structural Health Monitoring* (*Granada, Spain*) pp 987–95

[30] Bonnet M and Constantinescu A 2005 Inverse problems in elasticity *Inverse Problems* **21** R1–50

[31] Erdogan T 1997 Fiber grating spectra *J. Lightwave Technol.* **15** 1277–94

[32] Yamada M and Sakuda K 1987 Analysis of almost-periodic distributed feedback slab waveguides via a fundamental matrix approach *Appl. Opt.* **26** 3474–8

[33] Holland J H 1992 *Adaptation in Natural and Artificial Systems* (Cambridge, MA: MIT Press)

[34] Grefenstette J J 1986 Optimization of control parameters for genetic algorithms *IEEE Trans. Syst. Man Cybern.* **16** 122–8